Expelled grains from an unseen parent body around AU Microscopii

E. Sezestre, J.-C. Augereau, A. Boccaletti, P. Thébault

A&A 607, A65 (2017)
DOI: 10.1051/0004-6361/201731061

Astronomy & Astrophysics

Expelled grains from an unseen parent body around AU Microscopii

É. Sezestre[1], J.-C. Augereau[1], A. Boccaletti[2], and P. Thébault[2]

[1] Univ. Grenoble Alpes, CNRS, IPAG, 38000 Grenoble, France
e-mail: elie.sezestre@univ-grenoble-alpes.fr
[2] LESIA, Observatoire de Paris, CNRS, Université Paris Diderot, Université Pierre et Marie Curie, 5 place Jules Janssen, 92190 Meudon, France

Received 28 April 2017 / Accepted 10 September 2017

ABSTRACT

Context. Recent observations of the edge-on debris disk of AU Mic have revealed asymmetric, fast outward-moving arch-like structures above the disk midplane. Although asymmetries are frequent in debris disks, no model can readily explain the characteristics of these features.
Aims. We present a model aiming to reproduce the dynamics of these structures, more specifically their high projected speeds and their apparent position. We test the hypothesis of dust emitted by a point source and then expelled from the system by the strong stellar wind of this young M-type star. In this model we make the assumption that the dust grains follow the same dynamics as the structures, i.e., they are not local density enhancements.
Methods. We perform numerical simulations of test particle trajectories to explore the available parameter space, in particular the radial location R_0 of the dust producing parent body and the size of the dust grains as parameterized by the value of β (ratio of stellar wind and radiation pressure forces over gravitation). We consider the cases of a static and of an orbiting parent body.
Results. We find that for all considered scenarios (static or moving parent body), there is always a set of (R_0, β) parameters able to fit the observed features. The common characteristics of these solutions is that they all require a high value of β, of around 6. This means that the star is probably very active, and the grains composing the structures are submicronic in order for observable grains to reach such high β values. We find that the location of the hypothetical parent body is closer in than the planetesimal belt, around 8 ± 2 au (orbiting case) or 28 ± 7 au (static case). A nearly periodic process of dust emission appears, of 2 yr in the orbiting scenarios and 7 yr in the static case.
Conclusions. We show that the scenario of sequential dust releases by an unseen point-source parent body is able to explain the radial behavior of the observed structures. We predict the evolution of the structures to help future observations discriminate between the different parent body configurations that have been considered. In the orbiting parent body scenario, we expect new structures to appear on the northwest side of the disk in the coming years.

Key words. methods: numerical – stars: individual: AU Mic – stars: winds, outflows – planet-disk interactions

1. Introduction

AU Mic is an active M-type star, in the β Pictoris moving group, with an age of 23 ± 3 Myr (Mamajek & Bell 2014). Its debris disk, seen almost edge-on, was imaged for the first time by Kalas et al. (2004) in the optical. The dust seen in scattered light was shown to originate from collisional grinding of planetesimals arranged in a belt at ~35–40 au (Augereau & Beust 2006; Strubbe & Chiang 2006; Schüppler et al. 2015). The belt was later resolved by millimeter imaging (Wilner et al. 2012; MacGregor et al. 2013). Because the star is very active, the dynamics of the dust grains is believed to be strongly affected by the stellar wind.

Recently, Boccaletti et al. (2015) have revealed five fast-moving, arch-like vertical features in this disk in scattered light imaging with HST/STIS (Schneider et al. 2014) and VLT/SPHERE (Beuzit et al. 2008) at three different epochs. The five structures, named A to E, are shown in Fig. 1. They are identified in the 2010, 2011, and 2014 images, except for the A structure which was too close to the star in 2010. Curiously, these structures are all located on the same side of the disk and they all show an outward migration. For structures D and E the velocities are such that these features could match asymmetries identified in earlier multiple wavelength observations (Liu 2004; Krist et al. 2005; Metchev et al. 2005; Fitzgerald et al. 2007). Although they move outward, the arch-like structures seem stable in shape over a time span of a few years.

The projected speeds derived from the observations are displayed in Fig. 2, which shows that they increase with rising distance to the star. The two outermost, at least, are exceeding the local escape velocity. There is currently no theorical framework to readily explain this behavior (see, e.g., Matthews et al. 2014, for a recent review on debris disks). Any dynamical process involving copious amounts of gas, such as radiation-driven disk winds that may cause the grains to reach high velocities are excluded by the small amount of gas remaining around AU Mic (Roberge et al. 2005, fixed an upper limit of H_2 mass at 0.07 $M_\oplus$). Vertical resonances with a planetary companion can form arch-like structures, but they stay on a Keplerian orbit (analogous to the case of Saturn's moons; see, e.g., Weiss et al. 2009). Lindblad resonances can induce spiral density arms phase-locked with a perturber, but if each structure corresponds to an arm, they would be observed on both sides of

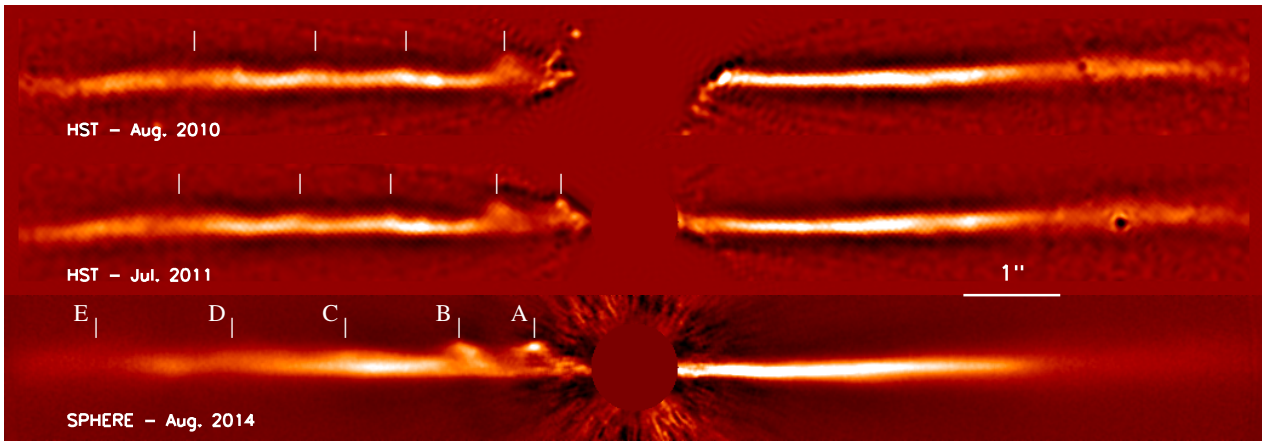

Fig. 1. 2010 and 2011 HST/STIS and 2014 VLT/SPHERE images of the debris disk of AU Mic. The five structures are identified in *the bottom panel*.

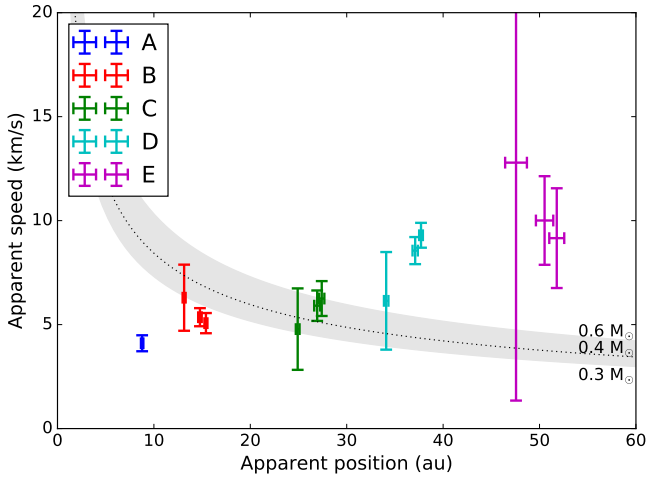

Fig. 2. Apparent speeds of the structures in the AU Mic debris disk derived from the observations (Tables 2 and A.1). The gray region shows the escape velocities for stellar masses ranging from 0.3 to 0.6 $M_\odot$, the dotted line corresponding to a mass of 0.4 $M_\odot$.

the disk. Concentric eccentric rings resulting from massive collisions of asteroid-like objects can produce local intensity maxima (e.g., Kral et al. 2015), but this process requires a time scale of 100 yr, while the structures escape the system in tens of years.

In this study, we aim to reproduce the observed high speeds and apparent positions of the structures. We leave aside the origin of the vertical elevation of the structures in this paper. In Sect. 2 we describe our model. There, we assume that the NW/SE asymmetry can be explained by a local process of dust release. This hypothetic emission source will be refered to as *parent body* in the following, without further specification. Boccaletti et al. (2015), for instance, proposed that this could correspond to a planet whose magnetosphere or dust circumplanetary ring would be interacting with the stellar wind. The dust released by the parent body is exposed to the stellar wind. The resulting wind pressure can put this dust on unbound trajectories, achieving the observed high projected speeds. In Sect. 3 we explore the case of a static parent body, which would for example mimic a source of dust due to a giant collision (e.g., Jackson et al. 2014; Kral et al. 2015) or a localized dust avalanche (Chiang & Fung 2017), and the case of an orbiting parent body, for example, a young planet. However, we emphasize that we do not suppose any specific dust production process in our study. Instead, we focus on the dynamical evolution of the dust right after its release, and any dust production mechanism will have to comply with the constraints we derive on the dust properties and dynamics. We discuss our findings, the influence of the parameters, and the implications in Sect. 4.

2. Model

We developed a model that aims to investigate the dynamics of dust particles released by a singular parent body and affected by a strong stellar wind pressure force. Throughout this paper, we make the important assumption that the observed displacements correspond to the actual proper motion of the particles and not to a wave pattern, which implies that the particles are supposed to have the same projected speeds as the observed structures. We discuss whether this assumption could lead to scenarios that reproduce the observed speeds in the AU Mic debris disk, and the conditions that must be fulfilled.

2.1. Parent body

To break the symmetry of the disk, we need an asymmetric process of dust production. The dust arranged in the fast-moving structures is thus assumed to be locally released by an unresolved, unknown source: the "parent body". This hypothetical parent body will not be described further, but we note that it must be massive enough to produce a significant amount of dust, although it should remain faint enough to be undetected by current instrumentation. Actually, the upper mass limit is fixed by the nondetection of point sources in SPHERE imaging. This implies a compact parent body smaller than 6 Jupiter masses beyond 10 au (see Methods in Boccaletti et al. 2015). The process of dust production is not described in this model, except that it must be sporadic otherwise we would observe one single, continuous feature. We can thus exclude the flares of the star as the trigger events responsible for the arch formation as they are too frequent (0.9 flare per hour following Kunkel 1973).

The parent body is assumed to be at a distance R_0 from the star in the plane of the main disk. When supposed to be revolving around the star, its orbit is considered to be circular. The dust particles are released with the local Keplerian speed.

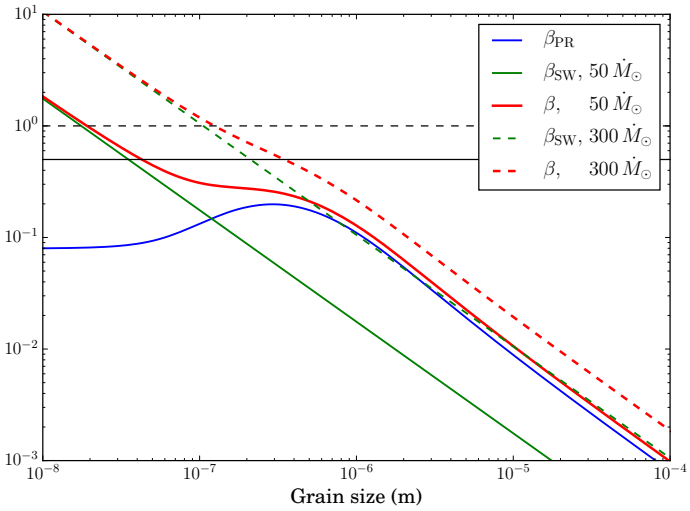

Fig. 3. β as a function of grain size. The material used for β_{PR} is M1 of Schüppler et al. (2015). Two hypothesis for the mass-loss rate of the star are shown (solid and dashed lines). The horizontal solid black line is the upper limit for bound trajectories assuming zero eccentricity for the parent body, and the dashed line is the limit between "normal" and "abnormal" parabolic trajectories (see Sect. 2.3).

2.2. Pressure forces

Assuming that the observed velocities correspond to the effective speeds of the particles, this means that they accelerate outward once released and finally exceed the escape velocity. As the particle size decreases, they are more affected by the pressure coming from the stellar wind. The radiation pressure is also more efficient, although it remains low because AU Mic is an M-type star. These processes can accelerate the particles outward, provided the total pressure force exceeds the gravitational force.

The two pressure forces are described by a single parameter denoted β in the following. It is the ratio of the wind plus radiation forces to the gravitational force

$$\beta = \frac{\|\boldsymbol{F}_{SW}\| + \|\boldsymbol{F}_{PR}\|}{\|\boldsymbol{F}_{grav}\|} = \beta_{SW} + \beta_{PR}, \quad (1)$$

under the assumption that the grain velocity v is such that $v \ll c$ and $v \ll V_{sw}$, where c is the light speed in vacuum and V_{sw} is the wind speed; $\boldsymbol{F}_{SW}$ is the force exerted by the stellar wind on the particle; $\boldsymbol{F}_{PR}$ is the radiation force, taking into account the radiation pressure and the Poynting-Robertson drag; and $\boldsymbol{F}_{grav}$ is the gravitational force of the star. For typical silicate submicrometer-sized grains, β ranges from $\sim 10^{-1}$ to a few tens (see Fig. 1 of Schüppler et al. 2015, and Fig. 11 of Augereau & Beust 2006).

The two contributions to β can be estimated with, for example, Eq. (28) of Augereau & Beust (2006) and Eq. (6) of Strubbe & Chiang (2006), respectively,

$$\beta_{SW} = \frac{3}{32\pi}\frac{\dot{M}_\star V_{sw} C_D}{G M_\star \rho s}, \quad (2)$$

$$\beta_{PR} = \frac{3}{16\pi}\frac{L_\star \langle Q_{PR}\rangle}{c\, G M_\star \rho s}, \text{ with } \langle Q_{PR}\rangle = \frac{\int_\lambda F_\lambda Q_{PR} \mathrm{d}\lambda}{\int_\lambda F_\lambda \mathrm{d}\lambda}, \quad (3)$$

where $\dot{M}_\star$ is the stellar mass-loss rate, C_D the dimensionless free molecular drag coefficient which has a value close to 2, G the gravitational constant, $M_\star$ the mass of the star, ρ the grain volumetric mass density, s the grain radius, $L_\star$ the stellar luminosity, Q_{PR} the dimensionless radiation pressure efficiency (which depends on the grain size, composition, and wavelength), and F_λ the stellar flux at wavelength λ.

The parameter β_{PR} is independent of the grain's distance to the star (r), but β_{SW} can slightly depend on r (e.g., Fig. 11 in Augereau & Beust 2006). In this study, we will neglect this effect. The value of β is highly size-dependent. For sufficiently large grains ($s \gtrsim 1$ μm in the case of AU Mic), β varies as s^{-1} (Schüppler et al. 2015). For smaller grain sizes, the relationship between β and s is more complex (e.g., Fig. 1 in Schüppler et al. 2015) and depends on the grain composition, the stellar mass-loss rate $\dot{M}_\star$, and the stellar wind speed V_{sw}. With $\dot{M}_\star = 50\,\dot{M}_\odot$ and $V_{sw} = V_{sw,\odot}$, the blowout size (grains with $\beta = 0.5$, assuming zero eccentricity for the parent body) is 0.04 μm (Fig. 3). This size jumps to 0.35 μm if the stellar mass-loss rate is increased to 300 $\dot{M}_\odot$. These values are consistent with those reported in Table 2 of Schüppler et al. (2015) although they differ slightly because of minor differences in the assumed stellar properties.

2.3. Particle behavior

The trajectory of a grain released from a parent body strongly depends on the β value. For a parent body on a circular orbit, the released $0 < \beta < 0.5$ dust particles remain on bound orbits, with eccentricities increasing with β, while the $0.5 < \beta < 1$ particles are placed on parabolic orbits. Dust particles with $\beta > 1$ will, on the other hand, follow unbound, "abnormal" parabolic trajectories, as described in, e.g., Krivov et al. (2006). These $\beta > 1$ grains are of particular interest in the context of the AU Mic debris disk because their velocites continuously increase while moving outward until they reach an asymptotic value, which can be evaluated by considering the total energy per unit of mass of the particle at a distance r from the star

$$e_m = \frac{1}{2}v^2 - \frac{GM_\star}{r}(1-\beta), \quad (4)$$

where $M_\star(1-\beta)$ is the apparent mass of the star. The particle is supposed to be released with the Keplerian velocity $v_0 = \sqrt{GM_\star/R_0}$ at radius R_0. Evaluating Eq. (4) in R_0 thus yields

$$e_m = \frac{GM_\star}{2R_0}(2\beta - 1)\,. \quad (5)$$

Therefore, the asymptotic speed reached by the dust particle far away from the star (valid for $\beta > 0.5$) is given by

$$v_\infty = v(r \to \infty) = \sqrt{(2\beta-1)\frac{GM_\star}{R_0}} = v_0\sqrt{2\beta - 1}. \quad (6)$$

For the $0.5 < \beta < 1$ grains, v_∞ is smaller than v_0. In this case, the asymptotic value of the velocity is reached by upper values and the speed decreases with the distance from the star. The $\beta > 1$ grains, on the other hand, reach the asymptotic value of the velocity by lower values, and v increases with r. This behavior is illustrated in Fig. 4. As shown in Fig. 2, the observed apparent speeds are not compatible with bound orbits at least for structures D and E. An unbound orbit is equivalent to $\beta > 0.5$ in the model. Furthermore, the overall trend of increasing velocity with the distance to the star is only reproduced by trajectories with $\beta > 1$ (see Fig. 4).

The strength of the pressure forces on the grains, characterized by β, and the released position of the grains, R_0, are two key parameters in this model, and some constraints on their values and relationship can be anticipated. For instance, if the grains

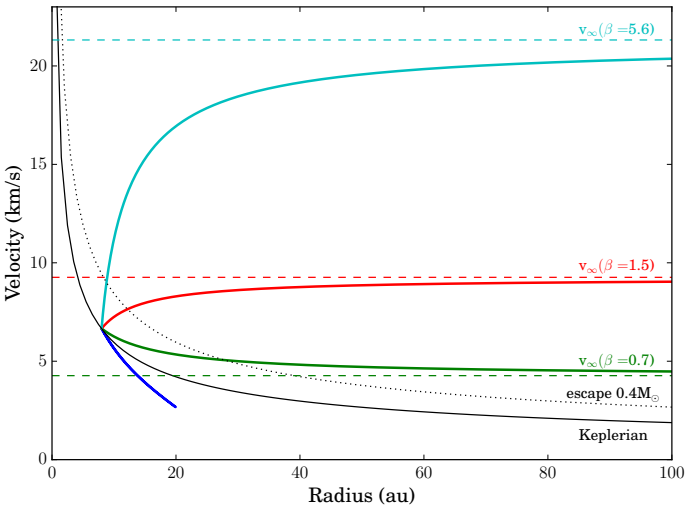

Fig. 4. Module of the velocity as a function of the distance from the star for a particle released with the Keplerian speed at 8 au. The solid curves correspond to $\beta = 0.3$ (blue), 0.7 (green), 1.5 (red), and 5.6 (cyan). The horizontal dashed lines are the asymptotic values of the velocity derived from Eq. (6).

Table 1. Documented stellar parameters of AU Microscopii (GJ803, HD 197481).

Parameter	Value	Reference
Spectral type	M1Ve	Torres et al. (2006)
Age	23 ± 3 Myr	Mamajek & Bell (2014)
Distance	9.94 ± 0.13 pc	Perryman et al. (1997)
Mass ($M_\star$)	0.3–0.6 $M_\odot$	Schüppler et al. (2015)
Wind speed (V_{sw})	4.5×10^5 m s^{-1}	Strubbe & Chiang (2006)

are on bound orbits ($\beta < 0.5$), their apoastron $r_a = (1 - 2\beta)^{-1} R_0$ should be sufficiently large for the particles to reach the position of the furthest structures, around 50 au in projection (structure E). Noting r_E the apparent position of the E structure, the condition $r_a \gtrsim r_E$ yields a strict lower limit on β:

$$\beta > \frac{r_E - R_0}{2 r_E}. \quad (7)$$

Nevertheless, we anticipate unbound orbits with high β values to best fit the observed speeds, and a power law linking β and R_0 can be approximated analytically. The trajectories of grains with β values much higher than 1 are almost radial and the limit speed reached by the particle is given by Eq. (6). The data points to reproduce are apparent speeds at projected distances. Let us take the pair (r_D, v_D) for structure D as an example, and denote α the angle between the observer and the direction of propagation of the particle. For a given projected distance r_D, the greater the released distance to the star R_0, the smaller the α angle. In a simple approximation, we can write that $\sin\alpha = r_D/(xR_0)$ by considering the right triangle, where r_D is the side opposed to the angle α and assuming the hypothenuse is x times R_0. Using Eq. (6) and the above approximation, the apparent speed writes

$$v_D \simeq v_\infty \sin\alpha \propto v_0 \sqrt{2\beta - 1} \cdot \frac{r_D}{R_0} \propto R_0^{-3/2} \sqrt{2\beta - 1}. \quad (8)$$

Therefore, we expect that, for a given observed velocity, the best fit solutions obey the following relationship between β and R_0,

$$(2\beta - 1) \propto R_0^3, \quad (9)$$

displayed as black lines in top left panel of Figs. 6, 7, and left panel of Fig. 8.

2.4. Parameters and numerical approach

We adopt the stellar parameters listed in Table 1. The stellar mass is not precisely determined, and we take $M_\star = 0.4\ M_\odot$, consistent with Schüppler et al. (2015) and the previous literature. The impact of the assumed stellar mass on the results is discussed in Sect. 4.2.2. For the wind speed, we adopt the value in the literature of 450 km s^{-1}, assumed to be constant with the distance from the star (see Strubbe & Chiang 2006; Schüppler et al. 2015).

Once these values are set, the particles' trajectories are fully determined by two parameters: the radius R_0 at which the grains are released, and the pressure to gravitational force ratio, β. To keep the problem simple, we suppose that all particles are submitted to the same pressure force, meaning that we consider only one particle size and a time-averaged value. The case of a range of β values is discussed in Sect. 4.2.3. In our model we assume that the dust release process takes place closer in than the planetesimal belt located at 35–40 au. We consider 40 values of R_0 ranging from 3 to 42 au, with a linear step of 1 au. The value of β is dependent upon the stellar activity. AU Mic is supposed to be on active state 10% of the time, with several eruptions per day. Augereau & Beust (2006) found values of β ranging from 0.4 in quiet state to 40 in flare state, with a temporal average value of typically 4 to 5 (see their Fig. 11). In our case, we consider 40 values of β ranging from 0.3 to 35 with a geometric progression in steps of ×1.13, and thus including bound orbits. It has been analytically demonstrated that considering a time-averaged value of β does not change the dust dynamics (see Appendix C of Augereau & Beust 2006), and we have numerically checked this behavior.

For numerical purposes, we work on a grid of (R_0, β) values and optimize the values of the other parameters to minimize χ^2. The trajectories are initially calculated for each pair (R_0, β) on the grid. A 4th order Runge-Kutta integrator, with a fixed default time-step equal to one one-hundredth of a year is used. The time resolution on the parent body orbit will nevertheless be reduced to 0.1 yr for numerical purposes in the case of an orbiting parent body. The calculation of a trajectory stops after two revolutions for the particle or for the parent body (if the particle has an unbound trajectory), or earlier if the dust particle goes farther than 200 au from the star. Then the computed trajectories are rotated with respect to the observer to account for projection effects. Another parameter θ is thus introduced, corresponding to the angle between the release point of the particle and the line of sight.

Two models are used in the following: one that assumes that the parent body is static and another where the parent body is rotating. In both cases, the parent body intermittently emits dust particles. In the static parent body model, the source of dust is static with respect to the observer as illustrated in the left panel of Fig. 5. The particles are all emitted with the same angle θ with respect to the observer, follow the same trajectory, and differ only by their release dates. In the other model, the parent body moves on its orbit, assumed circular, between each dust release event. Thus the angle of observation θ is linked to the release dates as shown in the right panel of Fig. 5. Two structures emitted with a time difference δt will be seen at an angle of $\omega\,\delta t$ from each other, where ω is the parent body angular velocity. We set apart a structure that we call reference structure. The angle of observation θ is defined with respect to this reference structure

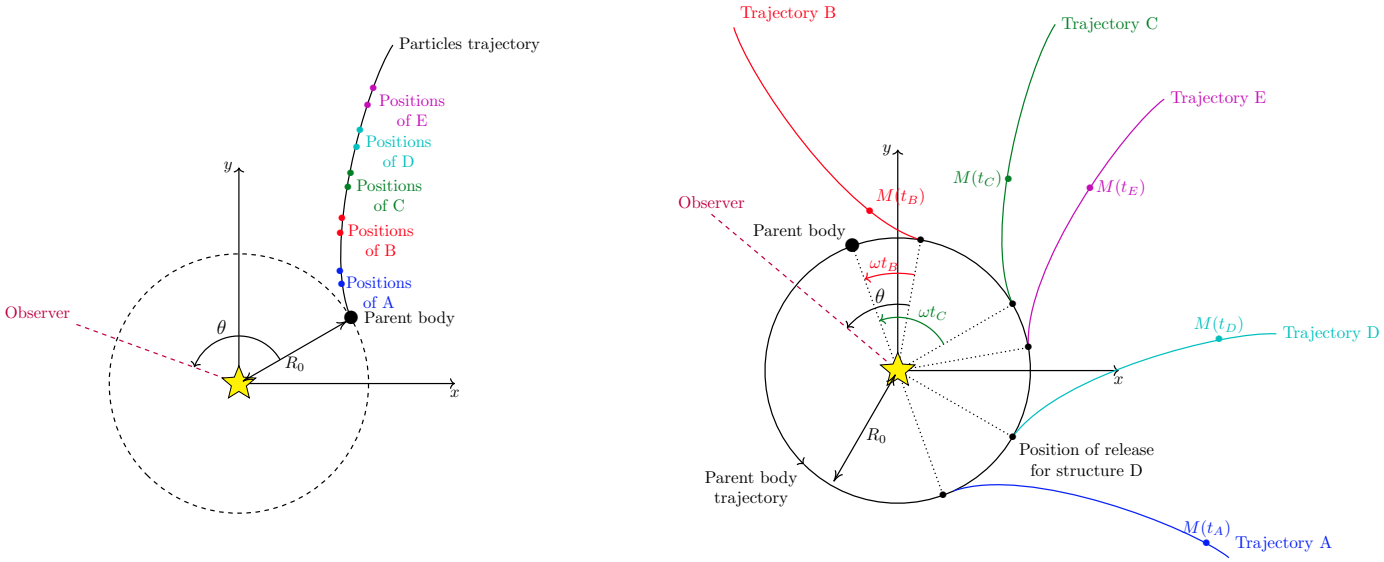

Fig. 5. *Left*: sketch of the static case, seen from above. *Right*: sketch of the orbiting case, seen from above. In this case, the structure B is used as the reference structure. The features are not necessarily emitted in alphabetical order.

Table 2. Apparent separations from the star (in arcseconds) of the maximum elevation from midplane of the five arch-like structures, named A to E, observed in the AU Mic debris disk in 2010, 2011, and 2014.

Date	A	B	C	D	E	Reference
2014.69	1.017 ± 0.025	1.714 ± 0.037	2.961 ± 0.073	4.096 ± 0.049	5.508 ± 0.074	Boccaletti et al. (2015)
2011.63	0.750 ± 0.025	1.384 ± 0.025	2.554 ± 0.025	3.491 ± 0.025	4.912 ± 0.208	Boccaletti et al. (2015)
2010.69	–	1.259 ± 0.037	2.459 ± 0.049	3.369 ± 0.061	4.658 ± 0.245	Boccaletti et al. (2015)
2004.75	–	–	–	2.52	3.22	Fitzgerald et al. (2007)
2004.58	–	–	–	2.52	3.12	Liu (2004)
2004.51	–	–	–	2.21	3.22	Metchev et al. (2005)
2004.34	–	–	–	2.62	3.32	Krist et al. (2005)
2004.545 ± 0.147	–	–	–	2.468 ± 0.154	3.220 ± 0.071	

Notes. In 2010, structure A is angularly too close to the star to be detectable. For consistency among all the features, the uncertainties on the positions of features A and B in 2011 have been re-estimated to twice their values, as published in Boccaletti et al. (2015). The next four rows give the positions of brightness enhancements (and not the maximum elevation positions) identified in 2004 and associated a posteriori to structures D and E. The last row shows the mean positions and uncertainties on the structures seen in 2004.

and all angles for the other structures are then deduced from the emission date.

In summary, the two models have a total of eight independent parameters: R_0, β, θ, and five dust release dates (one for each structure). For each fixed (R_0, β) pair, the code finds the position of the parent body that best matches the observations documented in Table 2 by adjusting the angle θ and the dust release dates. This is done by minimizing a χ^2 value that takes into account the uncertainties on the positions and also on the observing date in the specific case of the 2004 observations.

3. Results

We use the model described in the previous section to reproduce the apparent positions of the five structures observed at three epochs: 2010, 2011, and 2014 (see Table 2). We do not consider at this stage the 2004 observations because the positions of the structures were not derived using the same approach as for the other epochs. The consistency of our findings with the 2004 data is discussed in Sect. 4.2.1. We first consider the simple case of a static parent body (Sect. 3.1). Then we assume the parent body is revolving on a circular orbit around AU Mic (Sect. 3.2).

3.1. Static parent body

3.1.1. Nominal case

The simplest case to consider is that of a static parent body with active periods during which it releases dust particles. The reduced χ^2_r map of the fit to the apparent positions of the five structures over time is displayed in top left panel of Fig. 6. It shows two branches of solutions, which both follow the expected trend, namely β raising as R_0^3 (Eq. (9), solid and dashed black lines in top left panel of Fig. 6). As can be seen in bottom left panel of Fig. 6, the branch of solutions with the lowest R_0 values corresponds to particles expelled from the AU Mic system toward the observer ($0° \leq \theta \leq 90°$), while the branch with the highest R_0 values, which also contains the lowest χ^2_r values, corresponds to grains moving away from the observer ($90° \leq \theta \leq 180°$). This is illustrated in Fig. A.1. The best fit is obtained for the $\beta \simeq 10.4$ bin of the grid, corresponding to particles on unbound abnormal parabolic trajectories, as anticipated in Sect. 2.3.

The likeliest values of R_0 and β are derived using a statistical inference method by first transforming the map of unreduced χ^2 into a probability map assuming a Gaussian likelihood function

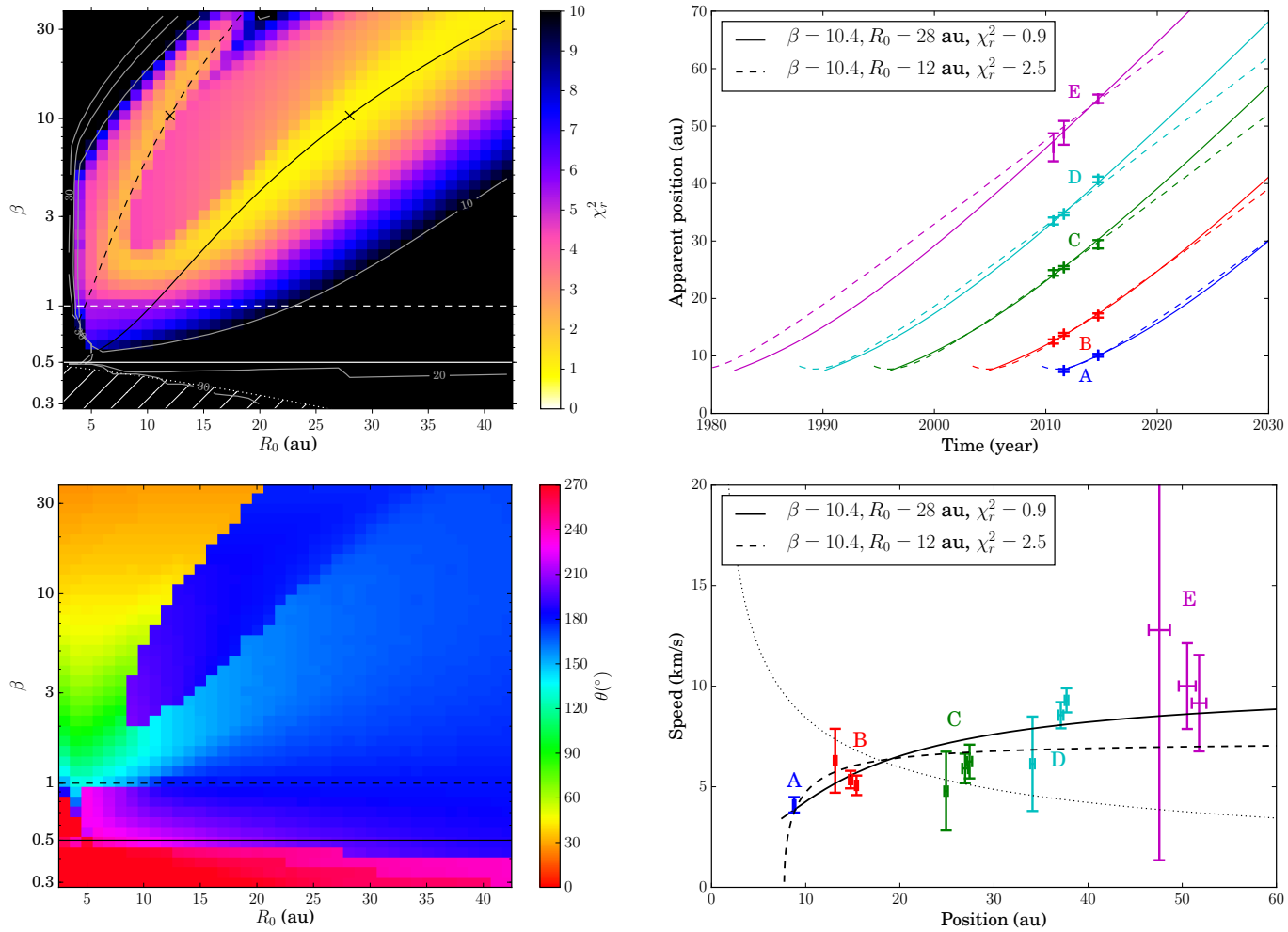

Fig. 6. Static parent body. Modeling results in the case of a static parent body. *Top left*: map of the reduced χ^2 (χ^2_r) obtained by fitting the position of the five structures. The solid and dashed black lines show the expected power law trends (Eq. (9)) along the two families of solutions, each scaled to go through the best fits identified by the black crosses. The branch of highest R_0 values corresponds to trajectories going away from the observer, while the other branch identifies the solutions pointing to the observer (see also Fig. A.1). The area under the dotted white line are solutions excluded by Eq. (7). *Bottom left*: map of the angle of emission, taken with respect to the observer. *Top right*: projected positions as a function of time. The solid lines correspond to trajectories going away from the observer, while the dashed lines are trajectories pointing toward the observer (see also deprojected trajectories seen from above in Fig. A.1). *Bottom right*: same as Fig. 2, overlaid with the best fit solutions (black crosses in *top left panel*).

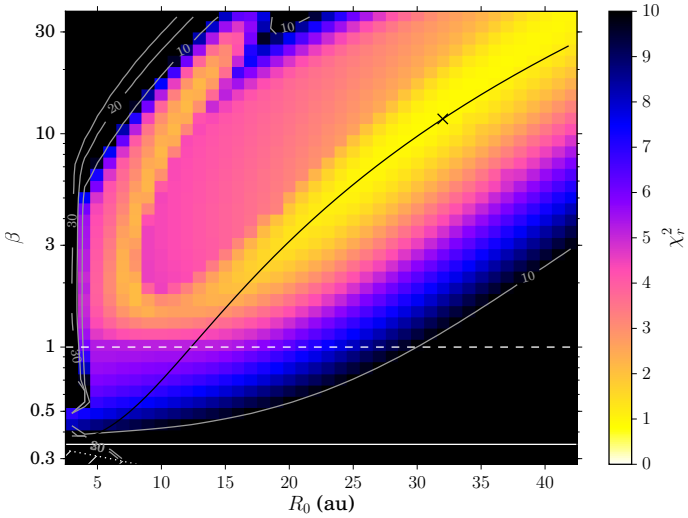

Fig. 7. Static parent body. Mean χ^2_r map for a parent body with an eccentricity of 0.3.

($\propto \exp(-\chi^2/2)$), and then by obtaining marginalized probability distributions for the parameters by projection onto each of the dimensions of the parameter space (see Figs. A.2 and A.3 in the orbiting case). This gives $\beta = 10.5^{+21.6}_{-4.5}$, $R_0 = 28.4^{+7.9}_{-6.8}$ au, and $\theta = 165 \pm 6^\circ$ (1σ uncertainties). The simulation closest to these values in the grid of models (right black cross in top left panel of Fig. 6, $\chi^2_r = 0.9$) is shown in the top and bottom right panels of Fig. 6, and the release dates of the particles are documented in Table 3. It shows a quasi-periodic behavior of about 7 yr, with the structures the closest to the star in projection being the youngest. Interestingly, we note that in this model the dust forming the A structure was released in mid-2011, which would be consistent with the nondetection of that feature in the 2010 HST/STIS data.

3.1.2. Eccentric orbits

At first glance, the case of a static parent body might appear a less physical situation than the case of an orbiting parent body. It could nevertheless correspond to a high-density region of large velocity dispersion in the aftermath of a giant collision. As

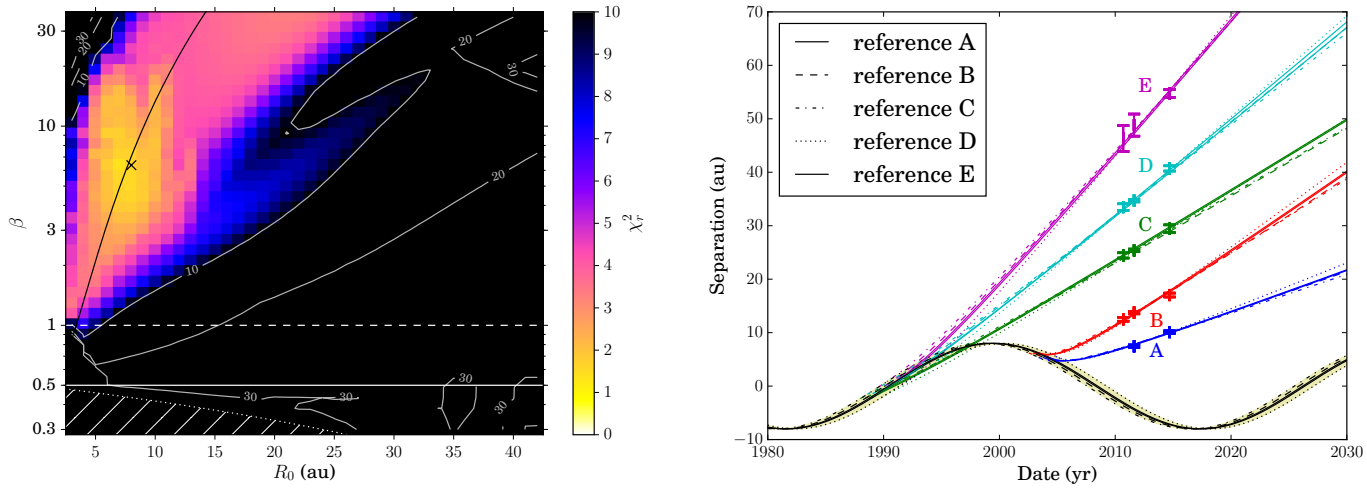

Fig. 8. Orbiting parent body. Modeling results of the position adjustment of all the structures in the case of an orbiting parent body (nominal case, see Sect. 3.2.1). *Left*: χ^2_r map averaged over the five references (see text). *Right*: projected trajectories for the five structures assuming each of the structures is a reference for the fit. This shows that the fits are essentially independent of the assumed reference structure. The black lines are the apparent positions of the parent body.

shown by Jackson et al. (2014) for example, the collision produces a swarm of large objects, passing through the same position in space, that will in turn become the parent bodies of the observed dust grains. This could mimic a static parent body, but importantly, the grains may be released from parent bodies on eccentric orbits. This will affect their initial velocity. Therefore, we test the impact of the parent body's eccentricity on the results by considering dust particles released at the pericenter position of parent body's orbit.

We arbitrarily consider parent bodies with an eccentricity of $e = 0.3$. The corresponding χ^2_r map is displayed in Fig. 7. The eccentricity lowers the limit between bound and unbound trajectories in terms of β. The total energy per mass unit becomes $e_m = \frac{GM_\star}{2R_0}(2\beta - 1 + e)$. In our case, the bound trajectories correspond to $\beta < 0.35$. The limit between normal and abnormal parabolic trajectories stay the same, $\beta = 1$. The power law in Eq. (9) is also modified, leading to $(2\beta - 1 + e) \propto R_0^3$. Introducing an eccentricity globally improves the fits (lower χ^2_r) at small β values, but does not change the best solutions significantly. The likeliest values of β and R_0 are respectively $12.1^{+17.7}_{-4.5}$ and $31.8^{+7.9}_{-4.8}$ au.

3.2. Orbiting parent body

3.2.1. Nominal case

We now consider the case of a parent body on a circular orbit. We assume a counterclockwise orbit when the system is seen from above, as illustrated in Fig. 9, but it was numerically checked that considering a clockwise orbit yields similar results, as expected (the x-axis is an axis of symmetry for the problem). The five structures are supposed to correspond to activity periods, when dust is released, occurring at different positions of the parent body on its orbit (Fig. 5, right panel). Therefore, each structure has its own trajectory although these are all self-similar in shape because they share the same R_0 and β values. For each (R_0, β) pair, we adjust the observed positions of the structures as a function of time, alternately considering each of the five structures as a reference structure in the fitting process (see Sect. 2.4 for details). This yields five fits to the data for any (R_0, β) pair; they appear to be consistent with each other, although with slight differences, and the results were averaged to derive a single χ^2_r map.

The results for an orbiting parent body are shown in Fig. 8. The χ^2_r map shows a region of best fits with β values similar to those found in the case of a static parent body, but for a dust release source much closer in. The likeliest values derived using the statistical inference method described in Sect. 3.1 are $\beta = 6.3^{+3.0}_{-2.4}$ and $R_0 = 7.7^{+1.0}_{-1.5}$ au. The closest solution in our grid of models is represented by the black cross on left panel of Fig. 8, namely $\beta = 6.4$ and $R_0 = 8$ au ($\chi^2_r = 1.7$). The corresponding projected trajectories for the five structures are displayed in the right panel of Fig. 8, showing an excellent agreement with the observations, independent of the reference structure used. We note, however, that the solutions are very close in terms of χ^2_r, and that additional observations are necessary to constrain the trajectory better.

From these results, we can derive a dust release date for each of the structures for the best fit model. These are listed in Table 3 (labeled "Orbiting free"), where the uncertainties combine the dispersion on the best ten percent pairs for a given reference structure, and the dispersion within the fits with the five different reference structures. In this model, structure C appears first (in ~1989), followed by D and E with an almost one-year periodicity. These three trajectories point in a direction opposite to the observer. Structures A and B, on the other hand, are released much later, in early 2000, about 10 to 15 yr after structure E. Their trajectories are furthermore oriented toward the observer. A face-on view of the five trajectories is displayed in the left panel of Fig. 9.

Although the one-year periodicity for structures C to E can provide some hints on the origin of the dust release process, the specific behavior of structures A and B suggests that caution should be taken about the interpretation of the model. This motivated us to test in the following the case of grouped release events for all the structures on a time span shorter than a quarter of the parent body's orbital period.

3.2.2. Grouped release events

We keep exploring the case of an orbiting parent body, but we now force the structures to be emitted more closely in time than

Table 3. Release dates (in years) of the structures A to E for the best fit for all the models considered.

	A	B	C	D	E
Static: $\beta = 10.4, R_0 = 28$ au					
Structure A as a reference	2011.6 ± 0.1	2005.0 ± 0.1	1996.2 ± 0.1	1990.3 ± 0.1	1982.2 ± 0.1
Structure B as a reference	2011.6 ± 0.1	2005.0 ± 0.1	1996.2 ± 0.1	1990.3 ± 0.1	1982.2 ± 0.1
Structure C as a reference	2011.6 ± 0.1	2005.0 ± 0.1	1996.1 ± 0.1	1990.2 ± 0.1	1982.1 ± 0.1
Structure D as a reference	2011.5 ± 0.1	2004.9 ± 0.1	1996.1 ± 0.1	1990.1 ± 0.1	1982.0 ± 0.1
Structure E as a reference	2011.4 ± 0.1	2004.8 ± 0.1	1996.0 ± 0.1	1990.0 ± 0.1	1981.9 ± 0.1
Average	2011.6 ± 0.1	2005.0 ± 0.1	1996.1 ± 0.1	1990.2 ± 0.1	1982.1 ± 0.1
Orbiting free: $\beta = 6.4, R_0 = 8$ au					
Structure A as a reference	2004.2 ± 0.6	2003.3 ± 0.9	1989.0 ± 0.7	1989.6 ± 0.7	1990.6 ± 0.7
Structure B as a reference	2003.7 ± 0.8	2002.9 ± 0.4	1988.4 ± 0.6	1989.0 ± 0.5	1990.0 ± 0.5
Structure C as a reference	2003.4 ± 0.6	2002.5 ± 0.6	1988.0 ± 0.3	1988.6 ± 0.1	1989.6 ± 0.2
Structure D as a reference	2004.9 ± 0.6	2003.9 ± 0.5	1989.8 ± 0.1	1990.5 ± 0.2	1991.6 ± 0.1
Structure E as a reference	2004.0 ± 0.6	2003.1 ± 0.5	1988.8 ± 0.2	1989.4 ± 0.2	1990.4 ± 0.2
Average	2004.1 ± 0.7	2003.1 ± 0.6	1989.1 ± 0.5	1989.3 ± 0.4	1990.6 ± 0.4
Orbiting frontward: $\beta = 24.4, R_0 = 17$ au					
Structure A as a reference	2000.8 ± 0.2	1999.4 ± 0.1	1997.2 ± 0.1	1995.8 ± 0.2	1994.1 ± 0.2
Structure B as a reference	2000.2 ± 0.1	1998.9 ± 0.1	1996.8 ± 0.1	1995.4 ± 0.1	1993.7 ± 0.2
Structure C as a reference	2000.4 ± 0.1	1999.1 ± 0.1	1996.9 ± 0.1	1995.5 ± 0.1	1993.8 ± 0.1
Structure D as a reference	2000.4 ± 0.2	1999.1 ± 0.1	1996.9 ± 0.1	1995.5 ± 0.1	1993.8 ± 0.1
Structure E as a reference	2000.3 ± 0.2	1999.0 ± 0.2	1996.9 ± 0.1	1995.5 ± 0.1	1993.8 ± 0.1
Average	2000.4 ± 0.2	1999.2 ± 0.1	1996.9 ± 0.1	1995.5 ± 0.1	1993.8 ± 0.1
Orbiting backward: $\beta = 5.6, R_0 = 8$ au					
Structure A as a reference	1990.7 ± 0.2	1991.1 ± 0.1	1992.1 ± 0.1	1993.0 ± 0.1	1994.5 ± 0.2
Structure B as a reference	1990.0 ± 0.1	1990.4 ± 0.1	1991.3 ± 0.1	1992.2 ± 0.1	1993.5 ± 0.1
Structure C as a reference	1989.7 ± 0.1	1990.1 ± 0.1	1991.0 ± 0.1	1991.8 ± 0.1	1993.1 ± 0.1
Structure D as a reference	1990.0 ± 0.1	1990.4 ± 0.1	1991.3 ± 0.1	1992.2 ± 0.1	1993.6 ± 0.1
Structure E as a reference	1989.6 ± 0.2	1990.0 ± 0.1	1990.8 ± 0.1	1991.6 ± 0.1	1993.0 ± 0.1
Average	1990.0 ± 0.2	1990.7 ± 0.2	1991.4 ± 0.2	1992.1 ± 0.2	1993.5 ± 0.3

Notes. The last row shows the average over the five reference structures. Uncertainties are derived from the dispersion of the results.

previously. This is achieved numerically by limiting the accessible range of dust release dates to a quarter of the parent body's orbital period. This leads to two situations: the case of five trajectories all oriented toward the observer on the one hand, and five trajectories all moving away from the observer on the other hand.

It turns out that none of these scenarios yields better fits to the data based on a χ^2_r criterion, which is expected since these situations were considered numerically in the nominal case (previous section). The best fit to the positions of the structures in time with particles forced to be emitted in the direction of the observer is shown in the middle panel of Fig. 9. It corresponds to $\beta = 24.7^{+10.6}_{-2.9}$, $R_0 = 17.3^{+4.7}_{-3.0}$ au, and the corresponding dust release dates are reproduced in Table 3. The fits with different reference structures are consistent with each other. The values of β and R_0 are significantly higher than those obtained in the nominal orbiting case (Sect. 3.2.1). The upper limit on β reaches the upper bound of the explored range in our simulations (see left panel of Fig. A.4), and we checked that expending this range increases the best β value, and the corresponding R_0 value in accordance with Eq. (9). The reduced χ^2_r of about 3.6 is worse than in the nominal orbiting case, but it is interesting to note that a dust release periodicity of about 1.5 yr does appear in this model, with the structures at the largest projected distances from the star being the oldest (release dates between about 1994 and 2000 for the E to A structures, respectively).

The case of particles forced away from the observer yields quite different results. The best fit is obtained for $\beta = 5.6^{+4.8}_{-3.6}$ and $R_0 = 8.1^{+2.0}_{-3.1}$ au (see right panel of Fig. 9), with a reduced χ^2_r value of around 3.5. In this case, the dispersion in the parameter values due to the use of different reference structures is greater than before, as can be seen in the right panel of Fig. 9. Overall, the mean β and R_0 values are similar to those in the nominal case (Sect. 3.2.1). The dust release dates are documented in Table 3. It shows that the periodicity is a little less than one year and the closest structures in projection are the oldest in this model; structure A appears in ~1990 and the structure E, the last, in ~1994.

In summary, even if the grouped emission solutions are not the best based on the χ^2_r criterion, they present the conceptual advantage of a periodicity.

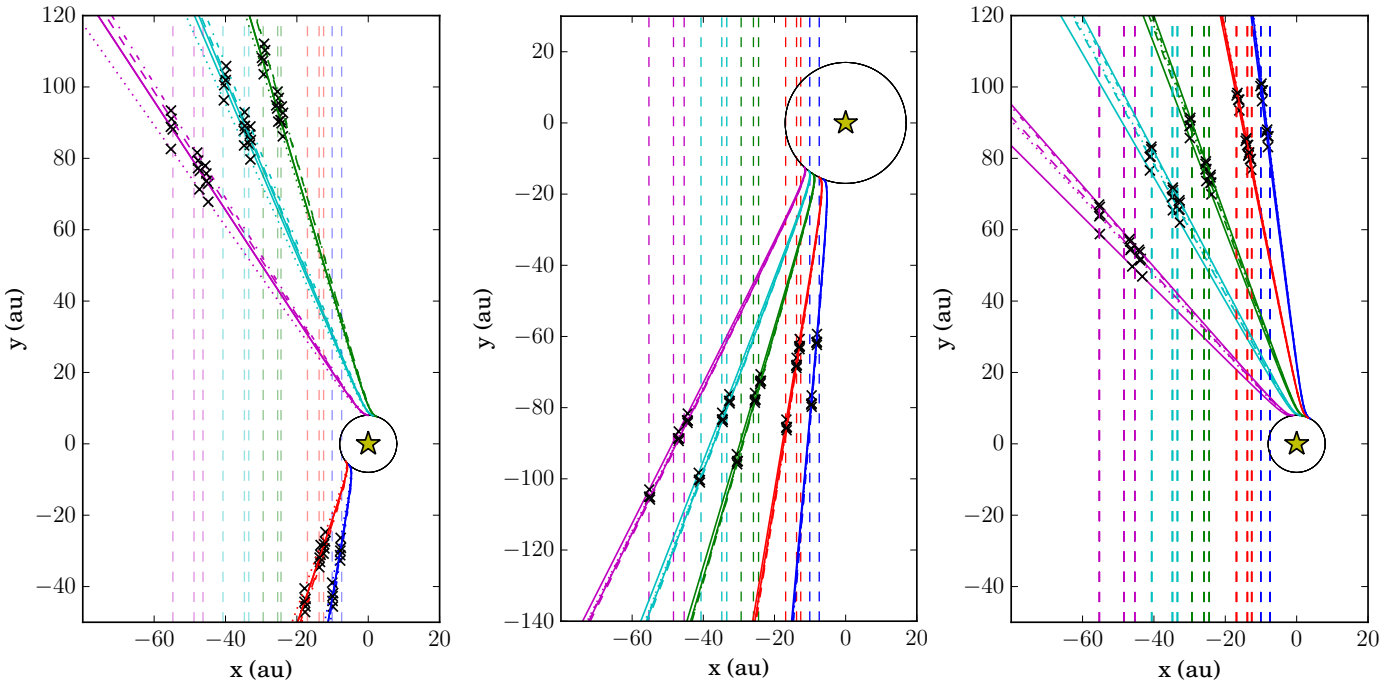

Fig. 9. Orbiting parent body. Trajectories of the particles seen from above for the five structures in the case of a rotating parent body (see Sects. 3.2.1 and 3.2.2 for details). *Left*: model without constraints. *Middle*: particles going toward the observer. *Right*: particles going away from the observer. For each structure five similar trajectories, sometimes superimposed, are displayed corresponding to best fits obtained when the reference structure is varied in the model. The color-coding is the same as in the previous figures. The solid black circle is the trajectory of the parent body. The crosses correspond to the observing dates.

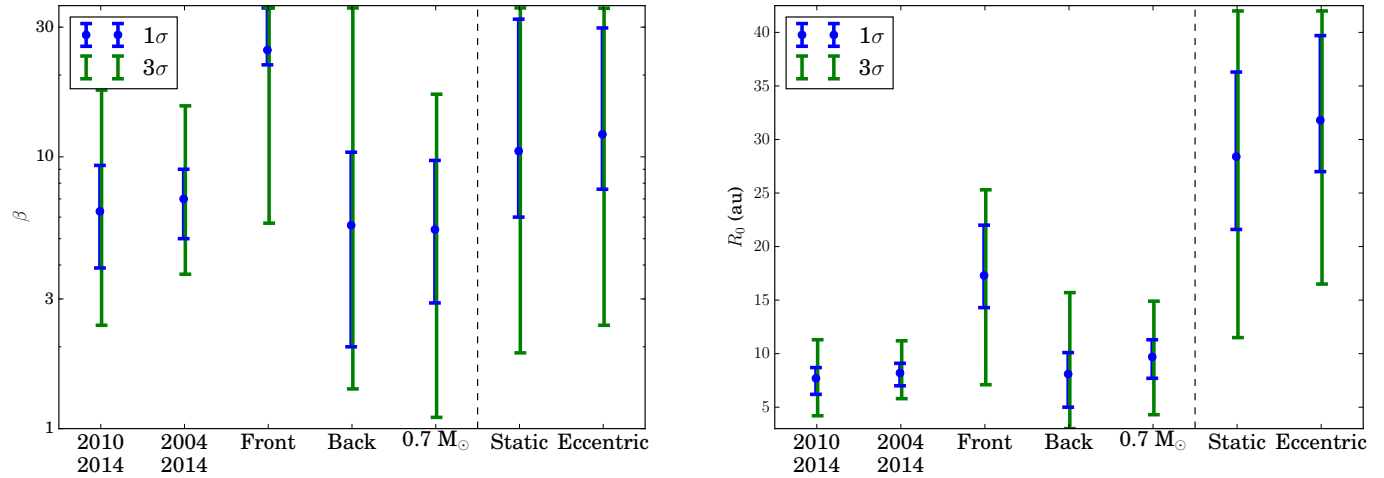

Fig. 10. *Left*: likeliest values of β depending on the model. "2010 2014" is the nominal orbiting case (Sect. 3.2.1); "2004 2014" is the same model, but taking into account the 2004 observations (Sect. 4.2.1); "Front" and "Back" are the grouped solutions (Sect. 3.2.2); "0.7 $M_\odot$" is the model with a stellar mass of 0.7 $M_\odot$ (Sect. 4.2.2); "Static" is the model of a static parent body (Sect. 3.1.1); and "Eccentric" is the model discussed in Sect. 3.1.2. *Right*: same, but for the dust release position R_0.

4. Discussion

4.1. Comparison between models

The simulations reproduce the general trend of increasing projected velocities of the structures with increasing distance to the star. This behavior can be explained by an outward acceleration of the particles being pushed away by a stellar wind pressure force that significantly overcomes the gravitational force of the star. The static and nominal orbiting parent body models provide equally good fits to the data. Figure 10 provides a digest of the β and R_0 values found in this study, along with the error bars at 1σ and 3σ. Our model requires the stellar wind to be strong enough to achieve β values typically between 3 and 10. In the static case, the dust seems to originate from a location just inside the planetesimal belt at 25–30 au from the star, while in the case of an orbiting parent body the best fit model is obtained for a dust release distance to the star R_0 of about 8 au. The release

dust events are less than 30 yr old, dating back to the late 1980s for the oldest, while the most recent features would have been emitted in mid-2000 at the latest in the case of an orbiting parent body, and as late as mid-2011 in the case of a static parent body. Some periodicity does appear in the simulations, but these depend on the model assumptions and current data are not sufficient to disentangle between the various scenarios considered in this study. For instance, the static parent body model shows a ~7-yr periodicity, while some 1- to 2-yr periodicities are found when considering an orbiting parent body with a possible 10- to 15-yr inactivity period in the best fit model (left panel of Fig. 9).

In the case of an unconstrained orbiting parent body, the best fit model suggests that structure C is older than structure D, which is itself older than structure E (Table 3 and left panel of Fig. 9). The observations would naively suggest the opposite, namely that the closest structures are the youngest. Indeed, the vertical amplitude of the arch-like structures seems to decrease with increasing apparent position (Boccaletti et al. 2015), suggesting for example a damping process when the structures move outward. The observed increase in the radial extent of the arches would also support this conclusion, although projection effects could also explain this behavior. In fact, independent of the scenarios displayed in Fig. 9, the orientation of the trajectories with respect to the observer are such that, should the arches have the same shape, their apparent radial extent would increase with increasing projected distance to the star, as observed. This criterion does not allow one scenario to be excluded, but ongoing follow-up observations could constrain the orientation of the structures with respect to the line of sight.

It is also worth mentioning that the case of grouped release events toward the observer (middle panel of Fig. 9) does yield surprising results that must be taken with care. For this case, the best fits tend to be obtained for the largest possible β values in our grid of models and extending the range of β values does confirm this trend. However, we note that the improvement in terms of χ^2_r is limited, and that fixing for instance β to about 6 would correspond to R_0 values close to 10 au ($\chi^2_r = 4.6$, see left panel of Fig. A.4), in better agreement with the other models. Therefore, in the following discussion, we adopt $\beta = 6 \pm 1$ and $R_0 = 8 \pm 2$ au as representative values in the case of an orbiting parent body, independently of whether the release events are grouped or not.

4.2. Critical assessment of the model

To assess the robustness of the model results, in the following we evaluate the impact of some assumptions on our findings.

4.2.1. Consistency with the 2004 observations

We have so far ignored the 2004 measurements since the arch-like features are not detected as such in these data sets. The presumed 2004 locations of the D and E features documented in Table 2 correspond to reported positions of brightness maxima in the literature rather than maximum elevations. On the other hand, these data greatly increase the time base and this provides an opportunity to check whether the brightness maxima identified in 2004 would be consistent with the dynamics of the D and E features that we inferred. We derived best fits to the combined 2004, 2010, 2011, and 2014 data by considering the case of an orbiting parent body with no restriction on the period of emission, a situation similar to the nominal case in Sect. 3.2.1. The likeliest values of β and R_0 are reported in Fig. 10 for comparison with those obtained previously. We find that adding the 2004 observations reduces the error bars, but has a marginal impact on the best values of the parameters (model labeled "2004 2014" in the figures). The best fit is indeed obtained for $\beta = 7.0^{+2.0}_{-1.8}$ and $R_0 = 8.2^{+0.9}_{-1.2}$ au. This compares well with the values derived from the best fit to the 2010–2014 data set, and introducing new data to the fit only yields a small increase in the reduced χ^2_r (2.4 vs. 1.7). Therefore, we conclude that the 2004 brightness asymmetries in the 2004 images can be associated with structures D and E, as proposed in Boccaletti et al. (2015). A more appropriate evaluation of these features will be presented in Boccaletti et al. (in prep.).

4.2.2. Stellar parameters

A parameter that can affect the modeling results is the stellar mass. The uncertainty on the estimation of AU Mic's mass leads us to examine the impact of a heavier star. We consider again the case of an orbiting parent body with no constraint on the emission dates, as in Sect. 3.2.1, and we change the stellar mass from 0.4 $M_\odot$ to 0.7 $M_\odot$ (labeled "0.7 $M_\odot$" in Fig. 10). The best value of β is essentially not affected ($5.4^{+4.3}_{-2.5}$), but R_0 is increased to $9.7^{+1.6}_{-2.0}$ au such that the orbital period is kept nearly constant with respect to the case of a lower stellar mass. In the 0.7 $M_\odot$ case, the parent body has an orbital period of 36.1 yr, against 33.8 yr in the solution of Sect. 3.2.1. It means that the time interval between each dust release event is more significant than the radius of emission. Overall, it shows that the uncertainty on the mass of the star does not significantly impact our main conclusions.

Another stellar parameter that can affect the simulations is the stellar wind speed, here assumed to be equal to the escape velocity at the surface of the star, following the approach by Strubbe & Chiang (2006) and Schüppler et al. (2015). Although observations (Lüftinger et al. 2015) and models (Wood et al. 2015) exist for the stellar wind of main-sequence solar-like stars of various ages, the constraints are very scarce for an active, young M-type star like AU Mic. In the literature, the values are either computed based on the escape velocity or by considering the temperature at the base of the open coronal field lines together with the Parker's hydrodynamical model (1958). This leads to wind speed values that can vary by a factor of up to 3 from one model to another. We have numerically checked that multiplying our adopted value of 450 km s^{-1} for the wind speed by a factor of 10 only changes the dust dynamics marginally. This is true as long as the dust speed is negligible with respect to the wind speed (see Sect. 2.2). As a consequence, the inferred best β and R_0 parameters are not affected by the exact V_{sw} value assumed in the model. However, the connection between β and the grain size depends on the wind speed, as discussed in Sect. 4.3.

4.2.3. β distribution and event duration

Our model intrinsically assumes that the observed features labeled A to E are made of grains of a single size (unique β value) and that the dust release events are sufficiently short in time to be considered instantaneous. In the case of an orbiting parent body, the best fit value for β shows a 1σ uncertainty of about 30%. That suggests a limited dispersion in β values. This is illustrated in the left panel of Fig. 11 which shows that a $\Delta\beta/\beta$ of about 1/3 can be tolerated as long as the D and E features are concerned, but the model becomes increasingly inconsistent with the observations when considering the features located closer and closer to the star. For the A, B, and C structures, we observe an overlap

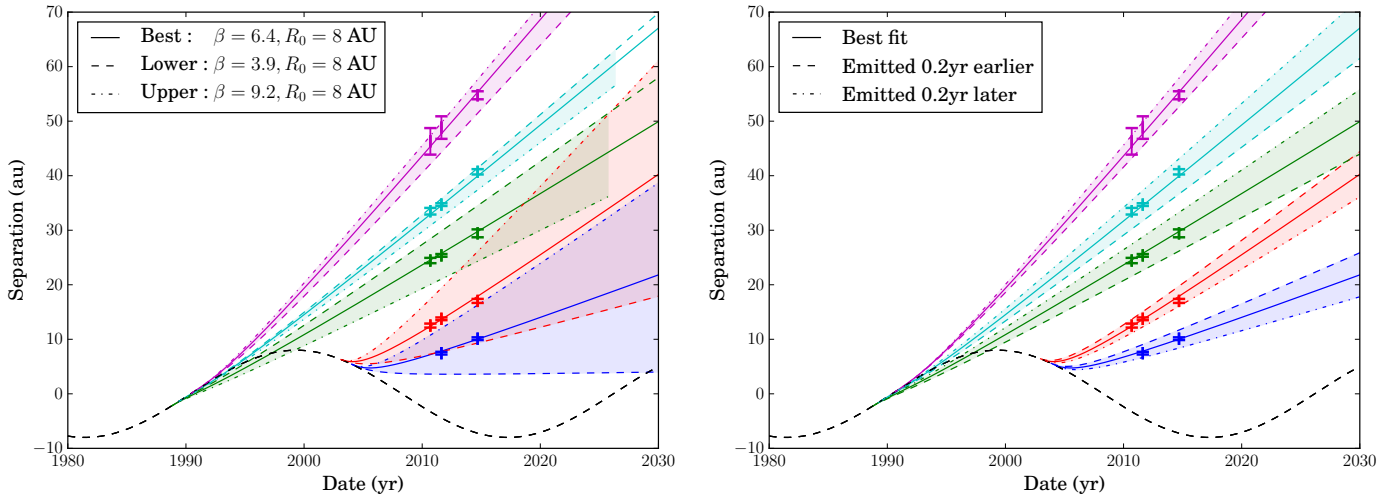

Fig. 11. Orbiting parent body. *Left*: spatial extent of the arches composed of particles with different β values emitted at the same date. *Right*: spatial extent of the structures composed of particles released continuously during 0.4 yr. The dashed black line corresponds to the apparent position of the parent body.

which connects the features, contradicting the observations. This very much suggests that either the arch-likes features are formed of grains with a narrow size distribution and/or that their cross sectional area is dominated by grains in a narrow size range (see also Sect. 4.3).

Likewise, assuming for example that the dust release events last a few months significantly widens the range of apparent trajectories as illustrated in Fig. 11 (right panel, $\Delta t = \pm 0.2$ yr). However, this behavior is still compatible with the observations since the structures are not mixed together and have a radial extent compatible with the one obtained here. This suggests that the emission process can occur during a few months, as long as it stays shorter than the time difference between two consecutive structures (0.6 yr in this case).

Therefore, the ongoing follow-up on this system will be critical to further constrain the β distribution and the duration of release events.

4.3. Grain size and mass loss rate

Our best fit value for β (about 6.3 in the case of a free orbiting parent body) is large enough to consider that the contribution of the radiation pressure to the dynamics of the grains forming the arch-like features can be neglected. Indeed, the low luminosity of the star means that $\beta_{\rm PR}$ never exceeds 0.3, as can be seen in Fig. 10 of Augereau & Beust (2006). Therefore, we can assume $\beta \simeq \beta_{\rm SW}$, and as a consequence, the link between β and the grain size s is degenerated with the mass-loss rate $\dot{M}_\star$ and the stellar wind speed $V_{\rm sw}$, such that $\beta \propto \dot{M}_\star V_{\rm sw}/s$ (Eq. (2)). This is illustrated in Fig. 12, using dust composition M1 of Schüppler et al. (2015) with $\rho = 1.78$ g cm^{-3} (see their Table 2).

In this context it is interesting to question which grain sizes are probed by the visible/near-IR scattered light observations. For the purposes of the discussion, we can approximate the dimensionless scattering efficiency $Q_{\rm sca}$ by a constant for grains much larger than the observing wavelength (geometric optics, $x \gg 1$ where $x = 2\pi s/\lambda$ is the size parameter), and $Q_{\rm sca} \propto x^4$ for small grains in the Rayleigh regime ($x \ll 1$). The differential scattering cross section, that writes $Q_{\rm sca}\pi s^2 {\rm d}n(s)$, is proportional to $s^{6+\kappa}{\rm d}s$ for $x \ll 1$ and $s^{2+\kappa}{\rm d}s$ for $x \gg 1$ when considering a power law differential grain size distribution ${\rm d}n \propto s^\kappa {\rm d}s$ with a lower cutoff size $s_{\rm min}$. For any value of κ such that $-7 < \kappa < -3$, like the classical collisional "equilibrium" size distribution in $\kappa = -3.5$[1], the scattering cross section will be dominated by grains such that $s \sim \lambda/2\pi$ (i.e., $x \sim 1$). The ranges of grain sizes that these correspond to are displayed in Fig. 12 for the HST/STIS (broadband, 0.2–1.1 μm), SPHERE/IRDIS (J-band), and SPHERE/ZIMPOL (I'-band) observations and are typically on the order of ~0.1 μm. In order for grains of this size to reach

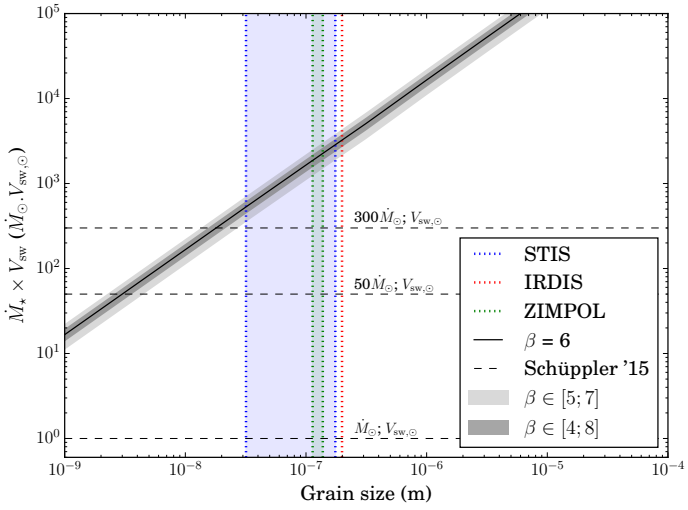

Fig. 12. Product of the mass-loss rate with the wind speed vs. grain size for the likeliest values of β obtained in our simulations. The gray areas correspond to the dispersion of β in the orbiting cases. For simplicity, our assumed value of wind speed of 450 km s^{-1} is labeled $V_{\rm sw,\odot}$. The colored vertical lines indicate, for each observing wavelength, the range of grain sizes corresponding to the smallest grains that efficiently scatter light ($s \sim \lambda/2\pi$) and which should dominate the flux for any "non-exotic" grain size distribution in the clumps (see Sect. 4.3 for details).

[1] However, such an equilibrium distribution might not apply across the $\beta = 0.5$ limit where a sharp transition is expected (Krivov 2010).

our likeliest β value of ~6, we need the $\dot{M}_\star \times V_{\rm sw}$ to reach values as high as a few 10^3 the solar analog. Such values are at least 20 times greater than the $50\,\dot{M}_\odot \times V_{\rm sw,\odot}$ derived by Schüppler et al. (2015) from collisional modeling of the overall disk. However, such very large values cannot be fully ruled out because there is a wide spread of $\dot{M}_\star V_{\rm sw}$ estimates reported in the literature for M-type stars, including values 3 to 4 orders of magnitude higher than the solar case (see, e.g., Vidotto et al. 2011, and references therein). The global trends of $\dot{M}_\star$ decreasing with age and increasing with stellar activity (Wood et al. 2005) favor a high mass-loss rate in the case of AU Mic.

It remains to be checked, however, whether the apparent positions and velocities are sensitive to the observing wavelength, which is difficult to conclude with the current data because the spectral range of the observations is limited. With a collisional grain size distribution, one would indeed expect that the structures at visible wavelengths might be formed of smaller grains with larger β values than the structures observed in the near-infrared (smaller β values). An alternative would be that the size distribution is very narrow, which can be schematically described by a steep size distribution with a minimum size cutoff. For $\kappa < -7$, the scattering cross section is always dominated by the smallest grains of the size distribution ($s_{\rm min}$), regardless of the observing wavelength. In this case, the features' measured positions and velocities would be the same at all wavelengths, and all images could be dominated by the same grain sizes, which could be much smaller than 0.1 μm and thus require relatively moderate $\dot{M}_\star V_{\rm sw}$, typically 10^2 the solar value. This would be consistent with the blue color of the overall disk, indicating a cross sectional area dominated by submicrometer-sized grains, while micrometer-sized grains would produce gray scattering (Augereau & Beust 2006; Fitzgerald et al. 2007; Lomax et al. 2017).

We conclude that either the features are formed of grains with a size distribution that is consistent with being collisional, thus requiring a high stellar mass-loss rate, or that they are formed of grains in a very narrow range around very small sizes ($\ll$0.1 μm) allowing moderate mass-loss rate but requiring a physical explanation for the presence of such a large amount of nano-grains and the relative absence of slightly bigger grains (because the size distribution is extremely peaked around $s_{\rm min}$).

4.4. Detected and undetected features

4.4.1. Future positions of observed features and parent body

Our model yields constraints on the spatial and temporal origin of the grains forming the fast-moving features. This can be used to predict the future positions of the structures and offers an opportunity to determine, with upcoming observations, which of the four scenarios discussed in this study is the best (see Fig. 13). Nevertheless, this figure clearly shows that the differences in apparent positions of the features according to the various scenarios start to become significant at least a few years after the most recent data used in this paper.

The predicted positions of the features for each model are documented in Table 4. In 2020 for instance, the predicted positions typically differ by a few au (a few 0.1″), which is in principle large enough to reject some of the proposed scenarios. However, we warn that these plausible positions of the features are idealized and do not take into account the uncertainties on the model parameters. In summary, the apparent trajectories of the known structures need to be followed in time and can be compared to our model predictions, but this might not be enough to identify within the next few years the most realistic scenario among the four presented in this paper.

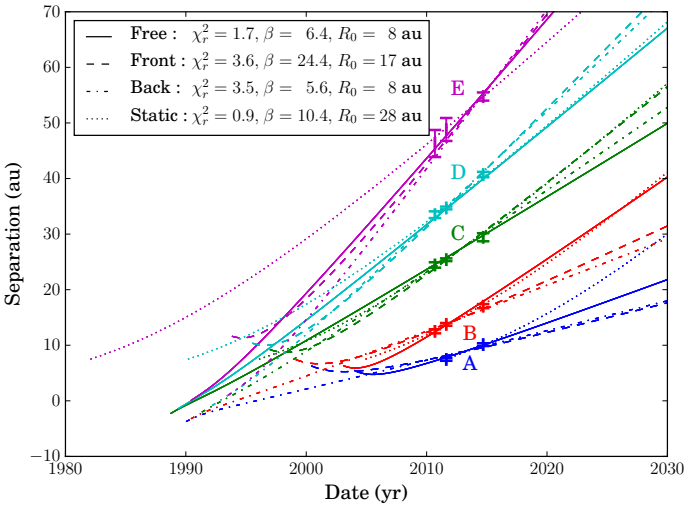

Fig. 13. Apparent positions of the features as a function of the observing date for the four optimal cases discussed in Sect. 3.

Interestingly, we note that, if its orbit is exactly seen edge-on, the unseen parent body should have transited or will at some point transit in front of the star. In all the parent body orbiting models, we expect it to have transited during the 2000–2014 time period if its orbit is counterclockwise. The free orbiting case predicts that the transit occurred in 2008.5, the frontward orbiting case predicts it in 2007.1, and the backward orbiting case in 2010.7. Light curves of the star taken during this period could show this hypothetical transit (although AU Mic is active). If the orbit is clockwise, the next transit is planned in 2026.4 in the free case, in 2062.5 in the frontward case, and in 2028.6 in the backward case.

4.4.2. Missing and future features

The observed structures are recent, and the dust release events occurred several times over the last 25–30 yr. Some scenarios are characterized with a pseudo-periodic behavior, which allows us to predict new structures to appear. Therefore, it is crucial to determine whether some additional features will be, or should have been, detected. In the static case for instance, we expect any new feature to be localized on the same side of the disk (southeast), and to be emitted with about a 7-yr periodicity (Sect. 3.1.1). This suggests that the next feature in the static case would be emitted between 2018 and 2020, and the evolution of its apparent position and projected speed should be similar to feature A, but shifted in time by about 7 yr. Perhaps more importantly, should any new structure be detected on the northwest side of the disk, the static parent body model would immediately be discarded.

To follow hypothetical new structures in the case of an orbiting parent body, in Fig. 14 we overplot snapshots of the dust grain positions at specific observing dates as if they were emitted continuously from the parent body. In the parent body rotating frame, these positions would correspond to streaklines. At a given observing date, any previously released structure should be located on this line. In the parent body orbiting model with ungrouped released events, the model suggests a period with little or no activity between about 1990 and 2000. Structures that would have been emitted during this time period would be

Table 4. Prediction of position (in arcseconds) for the five structures.

Date	Model	A	B	C	D	E
2015.0	Static	1.04 ± 0.01	1.78 ± 0.01	3.09 ± 0.03	4.09 ± 0.04	5.55 ± 0.02
	Orbiting free	1.03 ± 0.01	1.83 ± 0.02	2.97 ± 0.04	4.08 ± 0.03	5.63 ± 0.03
	Orbiting frontward	0.98 ± 0.01	1.69 ± 0.01	3.10 ± 0.02	4.20 ± 0.02	5.62 ± 0.01
	Orbiting backward	0.99 ± 0.03	1.66 ± 0.04	3.05 ± 0.01	4.19 ± 0.02	5.65 ± 0.01
2017.0	Static	1.24 ± 0.02	2.05 ± 0.01	3.42 ± 0.05	4.44 ± 0.07	5.93 ± 0.06
	Orbiting free	1.18 ± 0.02	2.11 ± 0.03	3.23 ± 0.05	4.44 ± 0.05	6.13 ± 0.04
	Orbiting frontward	1.08 ± 0.01	1.88 ± 0.01	3.44 ± 0.02	4.63 ± 0.02	6.17 ± 0.02
	Orbiting backward	1.10 ± 0.03	1.83 ± 0.04	3.35 ± 0.01	4.60 ± 0.04	6.23 ± 0.02
2020.0	Static	1.58 ± 0.03	2.49 ± 0.01	3.93 ± 0.08	4.98 ± 0.12	6.49 ± 0.12
	Orbiting free	1.41 ± 0.04	2.55 ± 0.06	3.62 ± 0.06	4.98 ± 0.08	6.90 ± 0.06
	Orbiting frontward	1.24 ± 0.01	2.17 ± 0.02	3.95 ± 0.03	5.29 ± 0.03	6.99 ± 0.03
	Orbiting backward	1.26 ± 0.04	2.08 ± 0.04	3.80 ± 0.03	5.23 ± 0.06	7.11 ± 0.05
2025.0	Static	2.25 ± 0.04	3.28 ± 0.04	4.82 ± 0.16	5.91 ± 0.21	7.45 ± 0.53
	Orbiting free	1.81 ± 0.07	3.30 ± 0.11	4.28 ± 0.07	5.89 ± 0.12	8.18 ± 0.11
	Orbiting frontward	1.50 ± 0.01	2.66 ± 0.02	4.81 ± 0.04	6.39 ± 0.05	8.38 ± 0.04
	Orbiting backward	1.53 ± 0.04	2.50 ± 0.05	4.54 ± 0.05	6.26 ± 0.09	8.58 ± 0.10

Notes. The uncertainties correspond to the dispersion due to the reference structure chosen.

located between 20 and 90 au in apparent separation from the star on the southeast side of the disk. Structures emitted after the most recent feature (feature A in about 2004) would have been too close to the star until 2012 to be detected with the available instrumentation (left panel of Fig. 14). After this date, new structures would be observable on the northwest side and would have been seen with VLT/SPHERE in 2014. Their nondetection could for instance suggest that the system entered a similar inactive period to that in 1990–2000.

In the scenario where all structures are moving away from the observer, the most recent structure (feature E) has been emitted late 1993, and new structures possibly emitted during the 1994–2010 time period would be observable on the southeast side of the disk, as shown on right panel of Fig. 14. Their nondetection suggests either that the process of dust release stopped for at least 15 yr or that the dust release process is much less efficient during that time interval, making the structures not observable (too faint, for example). Following the 2014 streakline, we also notice that no structure could be located farther than 70 au from the star in apparent separation in the images used in this study. The features possibly emitted after about 2010 would have been too close to the star to be detected until now, and this model predicts that new features could become observable on the northwest side of the disk in upcoming observations.

In the case of an orbiting parent body with grouped emissions toward the observer, the oldest structure was emitted in late 1993. Older features would be located beyond structure E in projection, and could have been too faint to be detected. Therefore, this model is consistent with the lack of more distant features in the HST/STIS images (the VLT/SPHERE field of view is limited to 6″), despite a possible 1.5- to 2-yr pseudo-periodicity (Sect. 3.2.2). The model also suggests that the most recent structure (feature A) is emitted in 2000, and middle panel of Fig. 14 shows that any feature formed during the 2000–2010 time period would be essentially lying along the line of sight to the star, yielding very small projected separations, preventing their detection with the VLT/SPHERE and HST/STIS images used in this paper. Therefore, the parent body could have continued emitting periodically since 2000 while remaining consistent with the nondetection of additional features. We note, however, that GPI observations by Wang et al. (2015) identified a source possibly corresponding to a compact clump of dust, within the apparent position of the A feature, and that would be consistent with a new structure emitted in 2001.1. Structures possibly emitted after 2011 should have been observed on the northwest side of the disk in 2014 (see the orange trajectory for the position of hypothetic structures arbitrarily emitted in 2012). This suggests again that either the pseudo-periodicity is too loose to predict precisely the arrival of future structures, or that the emission process has stopped. We note, however, that this orbiting parent body model remains the most consistent with a periodic behavior and the lack of detected features on the northwest side of the disk so far. Here again, a systematic monitoring is the key to addressing the actual evolution of the system.

5. Conclusion

We constructed a model to reproduce the apparent positions of the structures observed in the debris disk of AU Mic, taking into account the stellar wind and radiative pressure onto the dust grains, assuming that we observe the proper motion of the dust. We did not investigate the possible physical process at the origin of the dust production, but considered two different dynamical configurations for the release of the observed dust: a common origin from a fixed static location with respect to the observer, or release from a hypothetical parent body on a Keplerian orbit. In both cases, we find that the dust seems to originate from inside the planetesimal belt, at typically 8 au from the star in the best orbiting-parent-body model, or 28 au in the static case. The high projected velocities measured for each structure require that the observed grains have a high value of β (~6), the ratio

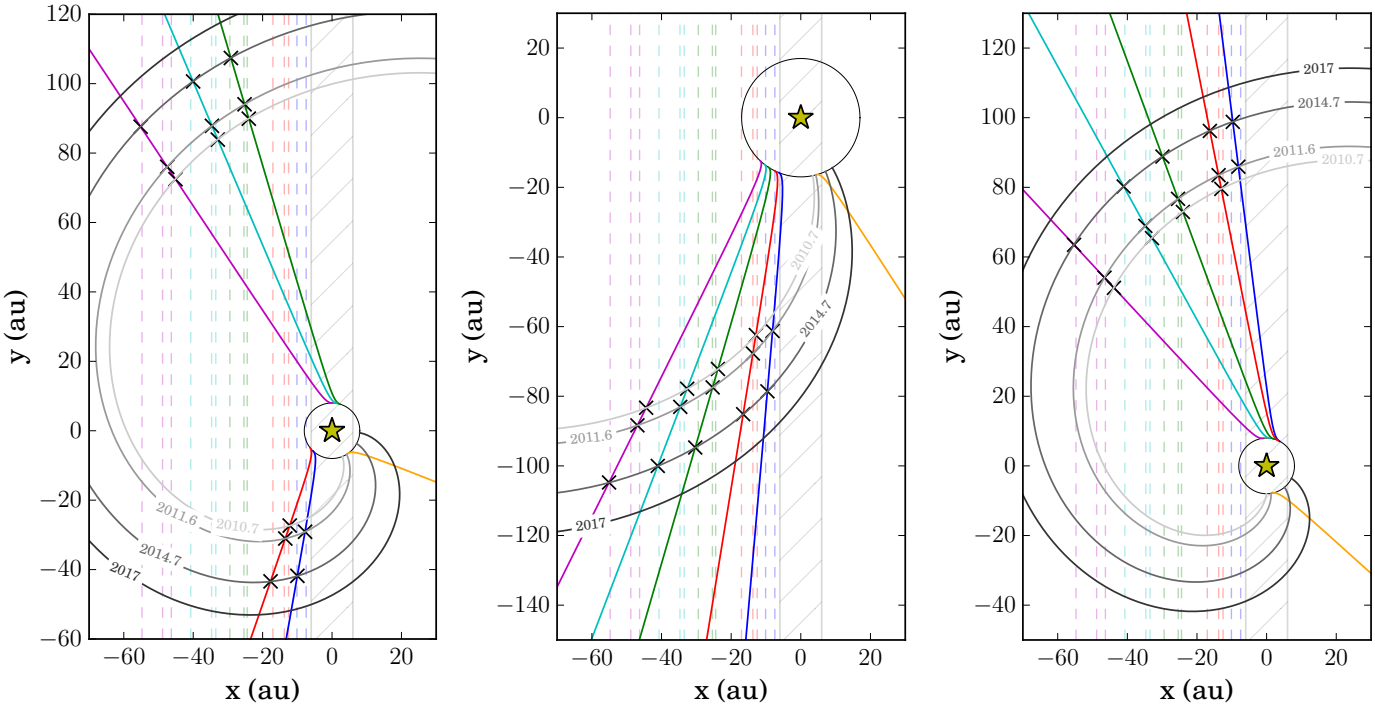

Fig. 14. Orbiting parent body. Trajectories of the particles seen from above averaged over the five reference structures (see Sects. 3.2.1 and 3.2.2, for details). *Left*: model without constraints. *Middle*: particles going toward the observer. *Right*: particles going away from the observer. The color-coding is the same as in the previous figures. The orange trajectory for the hypothetical particles released in 2012. The solid black circle is the trajectory of the parent body. The crosses correspond to the observing dates. The gray lines are the positions of the dust in 2010.7, 2011.6, 2014.7, and 2017 (from fainter to darker) if it was continuously emitted by the parent body on its orbit. The hatched area roughly corresponds to the masked inner region in the case of the STIS imager.

of pressure and radiative forces to the gravitational force. Our study could not disentangle all the scenarios considered based on the available observations. However, we were able to predict, for each scenario, the future behavior of the structures and we discuss the hypothetic appearance of new structures, especially on the northwest side of the disk. For all the scenarios, we find a semi-periodic behavior of dust release. We were also able to associate the brightness maxima observed in the 2004 images with the fast-moving structures resolved in the more recent high-contrast images. We suggest that the arch-like structures are either formed from ~0.1 μm-sized grains if the stellar wind is very strong, or from nanometer-sized grains ($\lesssim$20 nm) with a very narrow size distribution in the case of a more moderate stellar activity.

Our model does not provide direct constraints on the source of dust (parent body) or on the circumstances that yield to a release event. We can say, however, that it must be somewhat periodic, and that every release event should last less than 6 months. Furthermore, it must produce a great amount of submicron-sized grains, possibly with a narrow size distribution. Our static parent body model could correspond to planetesimals and dust formed after a giant collision, while an orbiting parent body could correspond to an unseen planet or a local concentration of dust due to resonant trapping with a planet, for instance. A process of accretion onto the parent body, leading to ejection (see, e.g., Joergens et al. 2013) can also be the origin of dust. The stellar wind plays a key role in our model and it is likely that the dust release events from the parent body are linked to the stellar activity. The stellar flares themselves are much too frequent to be the triggering process responsible for the feature formation. We speculate that this could be linked to the inversion of the magnetic field sign of AU Mic, and could help in forming arches (Sezestre & Augereau 2016; Chiang & Fung 2017). Overall, this model gives the base to a more complex model taking into account the vertical elevation of the structures that we will address in a future paper.

Acknowledgements. We thank Glenn Schneider and the HST/GO 12228 Team for the use of their reduced STIS image presented in Fig. 1. We thank the referee, Hervé Beust, Mickaël Bonnefoy, Quentin Kral, the VLT/SPHERE consortium team members, and the Exoplanètes team at IPAG for useful comments that helped in improving the paper. This work was supported by the "Programme National de Planétologie" (PNP) of CNRS/INSU co-funded by the CNES.

References

Augereau, J.-C., & Beust, H. 2006, A&A, 455, 987
Beuzit, J.-l., Feldt, M., Dohlen, K., et al. 2008, in Ground-based and Airborne Instrumentation for Astronomy II, Proc. SPIE, 7014, 701418
Boccaletti, A., Thalmann, C., Lagrange, A.-M., et al. 2015, Nature, 526, 230
Chiang, E., & Fung, J. 2017, ApJ, 848, 4
Fitzgerald, M. P., Kalas, P. G., Duchene, G., Pinte, C., & Graham, J. R. 2007, ApJ, 670, 536
Jackson, A. P., Wyatt, M. C., Bonsor, A., & Veras, D. 2014, MNRAS, 440, 3757
Joergens, V., Bonnefoy, M., Liu, Y., et al. 2013, A&A, 558, L7
Kalas, P., Liu, M. C., & Matthews, B. C. 2004, Science, 303, 1990
Kral, Q., Thébault, P., Augereau, J.-C., Boccaletti, A., & Charnoz, S. 2015, A&A, 573, A39
Krist, J. E., Ardila, D. R., Golimowski, D. A., et al. 2005, AJ, 129, 1008
Krivov, A. V. 2010, RA&A, 10, 383
Krivov, A. V., Löhne, T., & Sremčević, M. 2006, A&A, 455, 509
Kunkel, W. E. 1973, ApJSS, 25, 1

Liu, M. C. 2004, Science, 305, 1442
Lomax, J. R., Wisniewski, J. P., Donaldson, J. K., et al. 2017, ApJ, submitted [arXiv:1705.09291]
Lüftinger, T., Vidotto, A. A., & Johnstone, C. P. 2015, in Characterizing Stellar and Exoplanetary Environments, eds. H. Lammer, & M. Khodachenko (Springer International Publishing), 37
MacGregor, M. A., Wilner, D. J., Rosenfeld, K. A., et al. 2013, ApJ, 762, L21
Mamajek, E. E., & Bell, C. P. M. 2014, MNRAS, 445, 2169
Matthews, B. C., Krivov, A. V., Wyatt, M. C., Bryden, G., & Eiroa, C. 2014, Protostars and Planets VI (Tucson: University Arizona Press), 521
Metchev, S. A., Eisner, J. A., Hillenbrand, L. A., & Wolf, S. 2005, ApJ, 622, 451
Parker, E. N. 1958, ApJ 128, 664
Perryman, M. A. C., Lindegren, L., Kovalevsky, J., et al. 1997, A&A, 323, L49
Roberge, A., Weinberger, A. J., Redfield, S., & Feldman, P. D. 2005, ApJ, 626, 105
Schneider, G., Grady, C. A., Hines, D. C., et al. 2014, AJ, 148, 59
Schüppler, C., Löhne, T., Krivov, A. V., et al. 2015, A&A, 581, A97
Sezestre, É., & Augereau, J.-C. 2016, in SF2A-2016: Proceedings of the Annual meeting of the French Society of Astronomy and Astrophysics, eds. C. Reylé, J. Richard, L. Cambrésy, et al., 455
Strubbe, L. E., & Chiang, E. I. 2006, ApJ, 648, 652
Torres, C. A. O., Quast, G. R., Silva, L., et al. 2006, A&A, 460, 695
Vidotto, A., Jardine, M., Opher, M., et al. 2011, MNRAS, 412, 351
Wang, J. J., Graham, J. R., Pueyo, L., et al. 2015, ApJ, 811, L19
Weiss, J. W., Porco, C. C., & Tiscareno, M. S. 2009, AJ, 138, 272
Wilner, D. J., Andrews, S. M., MacGregor, M. A., & Meredith Hughes, A. 2012, ApJ, 749, L27
Wood, B. E., Müller, H.-R., Zank, G. P., Linsky, J. L., & Redfield, S. 2005, AJ, 628, 143
Wood, B. E., Linsky, J. L., & Güdel, M. 2015, in Characterizing Stellar and Exoplanetary Environments, eds. H. Lammer, & M. Khodachenko (Springer International Publishing), 19

Appendix A: Additional material

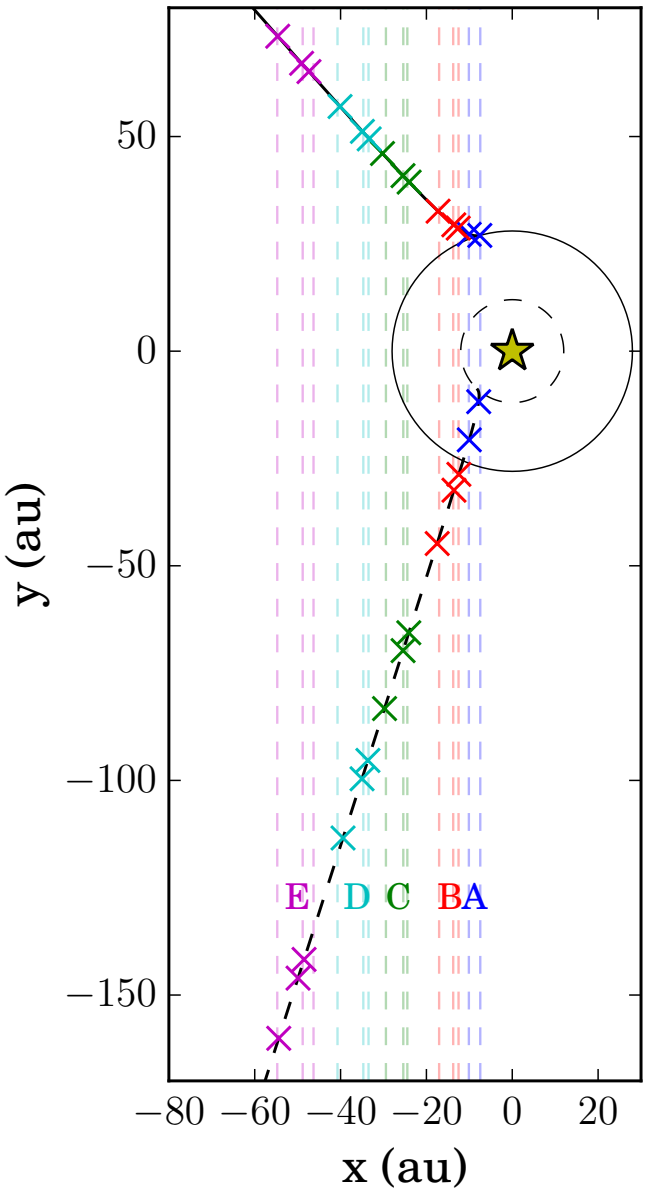

Fig. A.1. Static parent body. Trajectories of the particles seen from above that best fit the apparent positions (dashed lines, color-coding similar to Fig. 6) of five structures A, B, C, D, and E in the case of a static parent body. It corresponds to the trajectories plotted in black in top right panel of Fig. 6, namely (R_0, β, θ) = (28 au, 10.4, 165°) and (12 au, 10.4, 43°). The line of sight of the observer is assumed to lie along the y-axis in the direction of increasing y values, with the north-east side of the disk on the left.

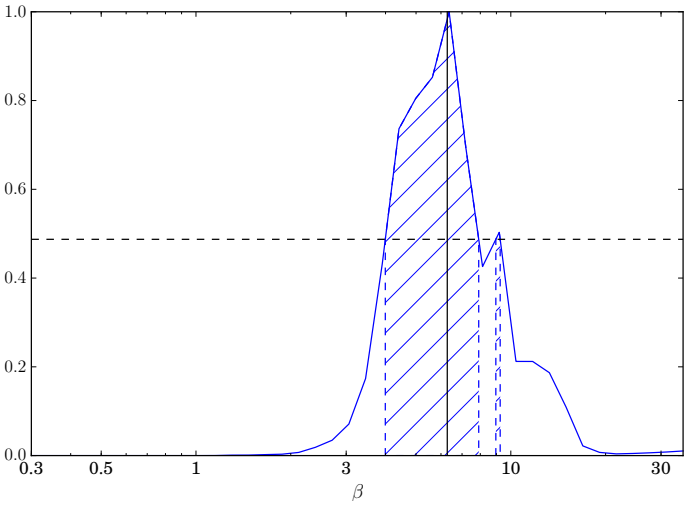

Fig. A.2. Orbiting parent body. Normalized probability distributions of β. The vertical black line is the mean value, and the dashed area corresponds to the 1σ distribution.

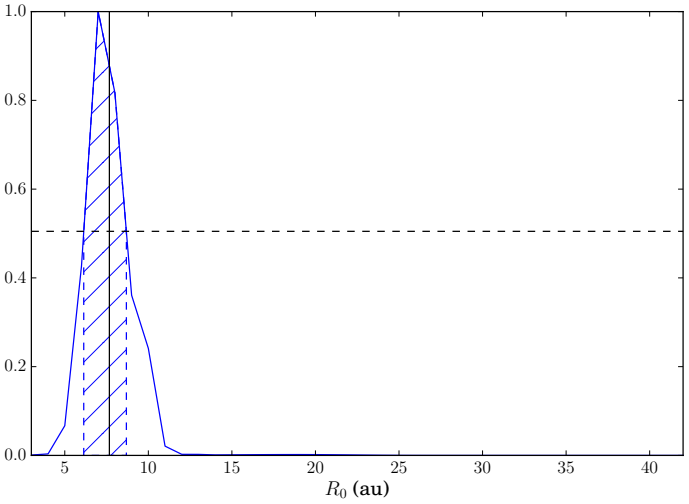

Fig. A.3. Orbiting parent body. Normalized probability distributions of R_0.

Table A.1. Positions and speeds of the five structures (A to E) at different epochs derived from the data in Table 2.

Epoch	Variable	A	B	C	D	E
2004–2010	x (au)	–	–	–	29.01	39.15
	δx (au)	–	–	–	0.58	0.90
	V (km s^{-1})	–	–	–	6.91	11.02
	δV (km s^{-1})	–	–	–	0.98	1.52
2004–2011	x (au)	–	–	–	29.62	40.42
	δx (au)	–	–	–	0.55	0.77
	V (km s^{-1})	–	–	–	6.81	11.26
	δV (km s^{-1})	–	–	–	0.81	1.17
2004–2014	x (au)	–	–	–	32.62	43.38
	δx (au)	–	–	–	0.57	0.36
	V (km s^{-1})	–	–	–	7.56	10.62
	δV (km s^{-1})	–	–	–	0.59	0.50
2010–2011	x (au)	–	13.14	24.91	34.09	47.56
	δx (au)	–	0.16	0.19	0.23	1.13
	V (km s^{-1})	–	6.29	4.78	6.14	12.79
	δV (km s^{-1})	–	1.59	1.96	2.35	11.44
2010–2014	x (au)	–	14.78	26.94	37.10	50.53
	δx (au)	–	0.18	0.31	0.27	0.90
	V (km s^{-1})	–	5.36	5.91	8.56	10.01
	δV (km s^{-1})	–	0.44	0.73	0.65	2.13
2011–2014	x (au)	8.78	15.40	27.41	37.71	51.79
	δx (au)	0.12	0.16	0.27	0.19	0.78
	V (km s^{-1})	4.10	5.07	6.25	9.30	9.16
	δV (km s^{-1})	0.38	0.49	0.84	0.60	2.40

Notes. Any position corresponds to a mean value over time. The values in this table are plotted in Fig. 2.

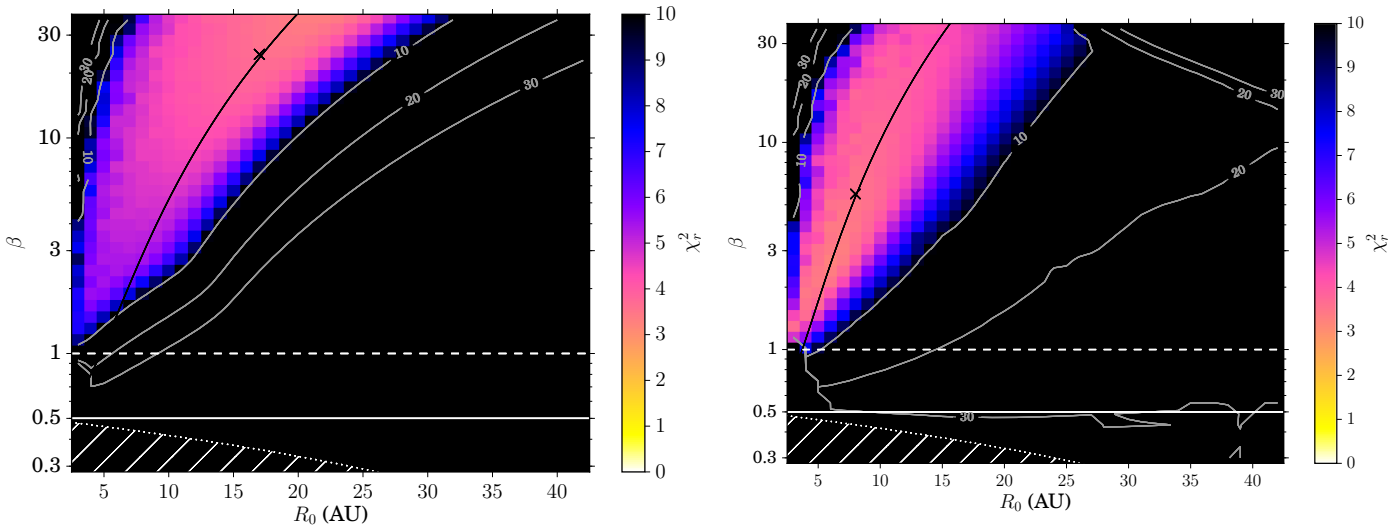

Fig. A.4. Orbiting parent body. χ^2_r maps for the grouped release cases. *Left*: forward case. *Right*: backward case.